# Prediction and Experimental Validation of Part Thermal History in Fused Filament Fabrication Additive Manufacturing Process

Mriganka Roy<sup>1</sup>, Reza Yavari<sup>4</sup>, Chi Zhou<sup>3</sup>, Olga Wodo<sup>1,2</sup>, and Prahalada Rao<sup>4\*</sup>

<sup>1</sup>Mechanical and Aerospace Engineering, University at Buffalo <sup>2</sup>Materials Design and Innovation, University at Buffalo <sup>3</sup>Industrial and System Engineering, University at Buffalo <sup>4</sup>Mechanical and Materials Engineering, University of Nebraska-Lincoln

#### Abstract

Part design and process parameters directly influence the instantaneous spatiotemporal distribution of temperature in parts made using additive manufacturing (AM) processes. The temporal evolution of temperature in AM parts is termed herein as the thermal profile or thermal history. The thermal profile of the part, in turn, governs the formation of defects, such as porosity and shape distortion. Accordingly, the goal of this work is to understand the effect of the process parameters and the geometry on the thermal profile in AM parts. As a step towards this goal, the objectives of this work are two-fold. First, to develop and apply a finite element-based framework that captures the transient thermal phenomena in the fused filament fabrication (FFF) additive manufacturing of acrylonitrile butadiene styrene (ABS) parts. Second, validate the model-derived thermal profiles with experimental in-process measurements of the temperature trends obtained under different material deposition speeds. In the specific context of FFF, this foray is the critical first-step towards understanding how and why the thermal profile directly affects the degree of bonding between adjacent roads (linear track of deposited material), which in turn determines the strength of the part, as well as, propensity to form defects, such as delamination. From the experimental validation perspective, we instrumented a Hyrel Hydra FFF machine with three noncontact infrared temperature sensors (thermocouples) located near the nozzle (extruder) of the machine. These sensors measure the surface temperature of a road as it is deposited. Test parts are printed under three different settings of feed rate, and subsequently, the temperature profiles acquired from the infrared thermocouples are juxtaposed against the model-derived temperature profiles. Comparison of the experimental and model-derived thermal profiles confirms a highdegree of correlation therein, with a mean absolute percentage error less than 6% (root mean squared error < 6 °C). This work thus presents one of the first efforts in validating thermal profiles in FFF via direct in-situ measurement of the temperature. In our future work, we will focus on predicting defects, such as delamination and inter-road porosity based on the thermal profile.

Keywords: Fused Filament Fabrication, Thermal History, Finite Element Modeling, In-process Temperature Measurement, Infrared Thermocouples.

<sup>\*</sup> Corresponding author. Email: rao@unl.edu

#### 1 Introduction

The overarching goal of this work is to understand the effect of the process parameters and part geometry (design) on the instantaneous spatiotemporal distribution of temperature – termed as the *thermal profile* or *thermal history* – in parts as they are being deposited layer-upon-layer using additive manufacturing processes. The knowledge of the causal factors that govern the thermal history of the part is the prerequisite for three important part functional quality-related aspects of additive manufacturing (AM) [1, 2]:

- Predict build defects, such as distortion and layer delamination, given the part geometry and a particular set of process conditions.
- Establish optimal process parameter settings and part design rules for a functional aspect, such
  as strength and geometric integrity.
- Institute closed-loop process control for defect mitigation.

Currently, the first two of the above three aspects in AM are realized mainly through empirical studies, which are time-consuming and prohibitively expensive. In a similar vein, process control in AM is primarily accomplished using sensor data-driven machine learning approaches which have limited capability for interpreting the underlying physical phenomena. An alternative strategy to purely data-driven process control is the so-called digital twin approach which aims to combine physics-based models of the AM process with in-process sensor data and analytics [3, 4].

As a step towards understanding the influence the thermal profile of AM parts on their quality, the objectives of this work are two-fold:

(1) Develop and apply a finite element-based framework that captures the transient thermal phenomena in a specific type of AM process called fused filament fabrication (FFF), (schematically exemplified in Figure 1).

(2) Validate the model-derived thermal profile with empirical in-process measurements of the temperature trends obtained under different experimental conditions.

The FFF process, which is classified under extrusion-based AM processes, is schematically shown in Figure 1 [5, 6]. FFF is the most popular and widely used AM process, given its simplicity, cost-effectiveness, and versatility of scale and materials. In FFF, typically, thermoplastic material in the form of a filament is heated past its glass transition temperature inside a nozzle (extruder). This semi-molten thermoplastic polymer is extruded through the nozzle and deposited as individual tracks (roads) onto a build table (bed). The part is built layer-upon-layer by translating the nozzle relative to the build table. On cooling, the extruded thermoplastic material (extrudate) bonds to the surrounding thermoplastic material deposited in previous passes [7].

Thermoplastic materials, such as acrylonitrile butadiene styrene (ABS) and polylactic acid (PLA) are accessible materials for FFF; however, a wide range of materials including carbon-fiber reinforced polymers, and non-polymer material, e.g., concrete and regolith can be processed using the extrusion-based method for material deposition [8, 9]. The specific material considered in this work is ABS, and the process condition varied is the feed rate setting, viz., the translation velocity of the extruder on the FFF machine, also called scan speed or deposition speed.

## Please Enter Figure 1 Here.

The salient aspects of this work, in the specific context of modeling and subsequent experimental validation of FFF process, are summarized hereunder:

 The deposition process is discretized in terms of finite elements at the level of individual tracks of deposited material (road-level). In other words, the model can be termed as quasicontinuous.

- To ensure accuracy, the model closely mimics the deposition process, in that, the movement of the nozzle in the x-y-z direction (called scan pattern or hatch pattern) is replicated in the model based on examination of the machine-level G-code. We note that the speed (feed rate) and path of the nozzle (scan pattern or hatch pattern) apart from the material-related aspects influence the cooling rate, and hence the thermal profile [10].
- From an experimental perspective, the thermal aspects of the process are monitored at the road-level using an array of in-process infrared non-contact thermocouple sensors. These sensors capture the thermal gradients on the top layer both ahead and behind the deposited material almost instantaneously.

The rest of this paper is organized as follows. We briefly summarize the prior works in thermal modeling and in-process measurement of thermal profile in FFF in Sec. 2. The computational model devised to understand the thermal profiles in FFF is described in Sec. 3. The experimental setup, including infrared thermal sensors and optical cameras are instrumented on a FFF machine, and the in-process data therefrom used to validate the model results are reported in Sec. 4. Finally, the conclusions from this work are summarized in Sec. 5.

#### 2 Literature Review

The literature review is divided into two parts. The first part summarizes the existing work in the area of theoretical modeling of the FFF process; the second part is dedicated to the literature in the sensor-based monitoring in FFF. The reader is referred to the two papers by Turner *et al.* which provide an in-depth review of modeling and process-structure-property relationships in extrusion-based AM processes, of which FFF is a major subset [11, 12].

## 2.1 Prior works in modeling thermal aspects of the FFF process.

Researchers have modeled various material-process interactions in the FFF process, namely, material behavior in the extruder [13], interactions between roads after their deposition [14], as well as mechanical [15], and thermal [16] aspects at various phenomenological scales [1].

The different phenomenological scales in FFF are classified as: (a) the bonding behavior of the deposited thermoplastic polymer, called polymer reptation [7], (b) physical deformation of the polymer during deposition, and (c) part-level aspects, such as warping due to residual stresses [17]. We herewith summarize the pioneering works in the area of thermal modeling in FFF.

Yardimci and Güçeri [14] were amongst the forerunners to have formulated an analytical framework to model the thermal behavior of the FFF process. The main objective for their work was to provide a fundamental understanding of the inter-road behavior of the material by performing the simulations for a single layer consisting of ten roads. For this purpose, they considered the thermal interactions between the deposited roads and accounted for their subsequent cooling and consolidation. Notably, they defined a bonding metric (i.e., bonding potential) to establish a qualitative measurement of the consolidation between roads. Their investigation, notwithstanding the elementary nature of the geometry studied, reveals that the bonding degree can vary within a single layer.

In another of their related works Yardimci et al. [13], through analytical modeling investigated the impact of the nozzle design on the output pressure, and subsequently established the mathematical formulations to assess the location of the meltpool (molten material in near the extruder) and the degree of cooling at the extruder tip. The focus was to establish the relationship between the meltpool and the feed speed, filament size, and material diffusivity. Through their investigation, a guideline to design the extruder tip, internal duct, and length of the heating

chamber (liquefier) depending on their effect on extrusion was established. This model is an example of an initial modeling effort to understand the effect of the extruder characteristics in FFF.

Another scope of the thermal interactions between the deposited roads in FFF was explored by Li [18]. They assumed the roads to be of semi-infinite length (as compared to the cross-section), which allowed them to study the impact of the local heat input on the entire printed part. Specifically, they used lumped capacitance analysis that assumes no spatial temperature variation in the zone of interest. They focused on the thermal behavior of a single road of length 50 mm and its influence on the entire part for different process parameters (extrusion temperature, envelope temperature, extruder tip size, road dimensions, fiber gap, and deposition pattern.). Through this investigation, they concluded that extrusion temperature and ambient temperature were the most important parameters that control the thermal profile.

A different tack to modeling in FFF was introduced by Rodríguez [19], who developed a finite element model to analyze the transient heat transfer in the printed parts. However, the part was relatively simple and consisted of only five vertically stacked roads. The next milestone was achieved by accounting for the behavior of the melt pool by Zhang and Chou [16]. They developed a three-dimensional thermal model of the melt-pool in FFF for a simple cuboid geometry with four layers consisting of 40 roads each. This model was later used by Zhang [17] to investigate the residual stress in FFF process. They related three parameters, namely, print speed, layer thickness and, road width, with the part distortion during a printing process demonstrating that scan speed is the most significant factor affecting the distortion. This numerical experiment was conducted on a specimen of size  $40 \times 10 \times 1.016$  mm (8 layers with 40 roads each).

Substantial progress on the modeling front was made by Costa et. al. [20], who studied the thermal conditions in FFF using ABAQUS® with particular emphasis on examining the effect of

convection and radiation (with the environment, entrapped air), and conduction (between the filaments and between the printed part and support) on the heat transfer phenomenon. They made the following important observations for subsequent models, including our model presented in this paper. They concluded that convection and conduction have the highest impact on the thermal profiles. Conversely, the convection and radiation in the air pockets between ellipsoidal filaments have a negligible effect. This observation reaffirmed justification for the assumption of the deposited road having a rectangular cross-section.

In recent years, several attempts have been made to introduce more computationally efficient models for thermal predictions, mostly for powder-based AM technologies, such as powder bed fusion and directed energy deposition. For instance, Pal *et al.* [21, 22] created a dynamic adaptive mesh refinement and de-refinement framework finite element approach to reduce the computation time in laser powder bed fusion. In their framework, the model utilizes a refined mesh in the region of the deposition to capture the large gradient in temperature, and a coarser mesh elsewhere as the deposition process progressing, thus, reducing the number of degrees of freedom, which in turn significantly reduces the computation time. The authors reported the ability to predict the thermal behavior 100 times faster than the traditional finite element models with a static mesh.

In a similar vein, Olleak *et al.* [23] created a thermo-mechanical model in the context of the laser powder bed fusion process using a dynamic re-meshing technique to capture the area in the vicinity of the meltpool with a higher accuracy using a finer mesh, compared to the rest of the part. Such an adaptive meshing approach is integral to commercial packages, such as Netfabb and 3DSim used for simulations in the laser powder bed fusion process [24, 25].

More recently, Yavari *et al.* [26, 27] proposed a mesh-less graph theoretic approach to model the thermal physics of metal powder-based AM process. The method eschews the time-consuming element

birth-and-death approach usually adopted in modeling AM. They verified the thermal history predictions from the graph-theoretic approach with Goldak's double ellipsoid moving heat source thermal model implemented in a finite element model. The graph-theoretic approach is shown to converge in a fraction (30 minutes versus over 3 hours) of the finite element implementation within error less than 6%.

In summary, several models to study the thermal behavior of layer-by-layer deposition in FFF have been proposed in the literature. In the juxtaposition of the literature, the extant gaps addressed by this work are as follows. First, the model proposed in this work is scaled to a large area, as opposed to the hatch-level – a critical step towards model-based closed-loop control in AM. Second, the model is validated with direct, in-process measurement of the temperature at the point where the material is deposited. Prior works in process modeling in FFF have resorted to indirect validation of the thermal trends by predicting the thermal-induced deformation.

## 2.2 Prior works concerning in-process monitoring in FFF.

In one of the earliest works in sensor-based monitoring in FFF, Bukkapatnam *et al.* [28] investigated vibration in FFF, comparing mechanistic lumped-mass models with experimentally obtained vibration sensor data, and demonstrated the ability to distinguish process abnormalities. Fang *et al.* [29] used machine vision techniques to detect defects in FFF of ceramics based on optical imaging of each layer during the build. Cheng and Jafari [30] examined the build surface using image intensity information and classified defects into two types, namely, randomly occurring defects, and anomalies due to assignable causes, e.g., improper extruder tool path. He *et al.* [31] studied on one of the common extruder nozzle clog problem in the FFF process with the help of the IR camera. They extracted features from IR camera images of each layer and analyzed to discern the nozzle from normal to clogged condition.

Wu et al. [32] applied the in-process acoustic emission sensing to collect the elastic waveform signals (acoustic emission). They concluded that the acoustic emission signals detect the two most common mechanical failure in FFF, namely, material run-out and filament breakage. However, the wide frequency range and high sampling rates of acoustic emission sensing process mandate high sampling frequency data acquisition, and moreover, is not related directed to the thermal aspects. In a similar vein, Rao et al. used a heterogeneous sensor array consisting of an IR thermocouple (similar to the one used in this work), multiple thermocouples, and an accelerometer to predict the onset of nozzle clogs in FFF. To explain further, the sensor data is used as an input in a statistical machine learning model to predict the onset of nozzle clogs as a result of a mismatch in material feed to flow rate ratios.

Seppala *et al.* [33] monitored the thermal behavior through IR imaging of the continuous deposition process and reported the cooling rate and time of consolidation through their observations. The thermal images acquired by Seppala were captured from the side (staring configuration) of the work, while in we focus on measuring the temperature of the freshly deposited extrudate as soon as it is deposited using infrared thermocouples mounted coaxial to the nozzle. In summary, the reported temperature measurements in Seppala *et al.* relate to layerwise analysis, while our work focuses on the freshly deposited extrudate on a hatch-by-hatch basis.

Dinwiddie *et al.* [34] acquired the temperature profile of the part during the printing process with two different thermal cameras. One was located outside of the chamber, behind a window. The other thermal camera was located inside the chamber and collected the reflection of the extruder tip from a gold mirror. Despite the expensive costs of two thermal cameras, another factor in FFF that hampers thermo-optical measurements in FFF is the small distance between the extruder tip and substrate. Kousiatza and Karalekas used the strain sensors and thermocouples as

their real time monitoring sensors at different layers of the printed part [35]. They reported that the magnitude of the induced residual strains has a direct correlation with the temperature field in the FFF process. Heretofore, monitoring the temperature profile of the process can be informative for quality assurance purposes. However, the fluctuations of the temperature are not prominently evident in the thermocouple sensors since top surface being deposited is at a much further location from the thermocouples as done. Thus, an infrared sensor, which is mounted to the extruder at a constant distance from the extruder tip during the printing, as implemented in this work is consequential and more informative to track the temperature profile at the top surface.

### 3 Transient Thermal Modeling of the FFF process

The degree of bonding of adjacent tracks deposited during the FFF process determines the functional integrity of the part, such as its strength, and is primarily governed by thermal aspects of polymer diffusion slightly above the glass transition region. In this regime, intermolecular forces in the polymer matrix are weak and adjacent extrudates (deposited material) form bonds through diffusion. When the temperature at the interface of two surfaces is higher than the glass transition temperature, the polymer-chains transition across surrounding surfaces through a process termed as *reptation* [36]. The strength of the bond is dependent on the average length of the polymers that penetrate through the interface, called minor chain length. The minor chain length, in turn, is a function of the temperature profile at the consolidating surface, and lastly, the heat flux governs the bonding degree. Following this reasoning, the part defects, e.g., delamination and warping, are a direct result of the poor bonding between adjacent extrudates, which in turn is contingent on the bonding temperature. Accordingly, predicting the thermal behavior of the deposited roads and quantifying its dependence on process parameters is consequential for determining the functional integrity of FFF parts.

#### 3.1 The mathematical formulation of the thermal model

In this section, we introduce the mathematical model that describes the thermal phenomena in FFF. To keep the development brief, the following assumptions are imposed:

- The nozzle is treated as a moving heat source, with the heat input originating from the extruded material deposited at high temperature.
- The material extruded is considered to be homogeneous and isotropic. The pores in the filament and possible change in density due to material vaporization are neglected.
- The material characteristics are assumed to be static, in that the specific heat capacity, density,
   and conductivity are considered to be temperature independent.
- The latent heat generated due to the change in the material from a liquid to solid-state is not considered.
- The shape of the filament deposited is assumed to remain identical. In other words, the shrinkage in the material due to cooling is neglected. Likewise, the effect of warping and distortion on the shape of the deposited roads are not accounted in the simulation.
- The ambient temperature  $(T_{am})$  and base temperature  $T_b$  are considered to remain constant during the process.

The main thermal heat transfer phenomena in FFF as per the different interaction zones are depicted in Figure 2, these are further delineated hereunder.

## Please Enter Figure 2 Here.

(1) Part-Substrate (Bed) Interaction Zone: The part is deposited on a substrate (in this work painters' tape) which is heated through a heater integrated inside the bed. The heating of the substrate prevents uneven cooling of the part and hence avoids thermal stress-related warping.

The heat transfer mechanism in this zone of the part corresponds to heat conduction with additional heat source supplied through table. In this work, the bed is maintained at 85 °C (358.15 K). We note that there is a control mechanism in the resistance heater provided in the aluminum heat bed on the Hyrel Hydra that is activated when the set temperature is outside a threshold (roughly 2 °C).

- (2) Part-Part Interaction Zone: As new semi-molten material is added, it contacts the previously deposited tracks (roads). Heat is transferred between roads and layers within the part through conductive heat transfer under the assumption of perfect contact between individual adjacent roads.
- (3) Part-Chamber Interaction Zone: The heat is dissipated from the free surfaces of the part into the chamber due to radiation and convection. Whilst in some FFF systems the chamber is heated; however, in this work, the chamber was not heated but was enclosed and maintained at an ambient temperature of 30 °C (303.15 K).
- (4) Part-Extruder Interaction Zone: Cool air is often blown over the freshly deposited semi-molten material from a fan integral to the extruder to aid quick solidification. This feature is valuable while building long unsupported spans (overhang features). Thus, heat transfer via forced convection takes place between the part and chamber due to the air blowing over the part. This fan was not active for a significant duration of the experiments in this work. Furthermore, there is another fan directed at the extruder (not the part) to avoid overheating of the extruder. This fan is assumed not to influence the process.
- (5) Part-Extruder Interaction Zone: At the point where the material is deposited, three heat transfer-related phenomena are active, these are: (i) heating of the part due to the extruder (treated as a moving heat source transferred through deposited material at a higher

temperature), (ii) latent heat generation due to material solidification, and (iii) the convection within the molten material before it solidifies. In this work, we ignored the latent heat and convection effects within the meltpool.

The factors that affect these phenomena comprise material properties, ambient temperature, deposition speed, part geometry and associated layer thickness, as well as deposition pattern. The model used in this paper accounts for these factors and thermal phenomena.

The thermal behavior within the deposited material is mathematically represented by the transient heat equation:

$$\rho c_p \frac{\partial T}{\partial t} = \nabla (\lambda \nabla T) + \dot{q} \quad in \Omega(t)$$
 (1)

where, T is the temperature,  $\rho$  is the density of the deposited material (kg/m³),  $c_p$  is the specific heat capacity (J/kg·K),  $\lambda$  is the thermal conductivity (W/m·K) and q represents the external heat source per unit volume (J/m³). The computation domain  $\Omega(t)$  evolves with deposition and hence is a function of time. In other words, the part geometry changes as the material is deposited, this is accounted through the element birth-and-death simulation schema in finite element.

$$\Omega(t) = f_{\Omega}(t) \tag{2}$$

The interaction of the printed material with the environment is considered as a boundary condition. The heat is dissipated through free surfaces of the printed part to the environment (by convection and radiation). This effect is modeled as a boundary condition applied on all free outer surfaces of the printed part given by the following equation:

$$q_{surf} = h(T - T_{am}) + \kappa (T^4 - T_{\infty}) \quad on \Gamma_f(t)$$
 (3)

where, h is the heat convection coefficient (W/m<sup>2</sup>·K) of the material at the ambient temperature,  $\kappa$  is the emissivity of air. Temperature  $T_{am}$  is the printing chamber temperature (K) during the

print,  $T_{\infty}$  is the reference temperature (K) at an infinite distance for radiation. The ambient temperature is assumed to be minutely affected by the deposition and hence,  $T_{am} = T_{\infty}$ .

However, as explained before, the free surfaces ( $\Gamma_f(t)$ ) evolves with time as more material is added to the printed part. When new roads are added, new surfaces are exposed to the cooling, consequently the free surfaces need to be updated in the model. At the same time, some of the surfaces are covered with newly added material and are no longer subjected to these boundary conditions, and they need to be removed from the model.

Typically, in most FFF machines, the bed is heated to avoid uneven cooling of the part, which is modeled by imposing constant temperature  $T_b$  through following boundary condition:

$$T_{\Gamma}(t) = T_b \quad on \, \Gamma_b(t)$$
 (4)

Similar to the previous boundary condition, the base surface changes with deposition time. However, in this case, the surface needs to be updated until the first layer is completely deposited, which is encapsulated as:

$$\Gamma_{b}(t) = \begin{cases} f_{\Gamma}(t) & \forall \ 0 \le t \le t_{layer} \\ f_{\Gamma}(t_{base}) & \forall t > t_{layer} \end{cases}$$
 (5)

where,  $t_{base}$  is the time required for the first layer to be printed.

The temperature of the locally added volume is set to the deposition temperature  $T_d$ :

$$T(t_d) = T_d \quad in \Omega(t) \tag{6}$$

In summary, the mathematical model consists of the governing equation Eqn. (1), two boundary conditions Eqn. (3) and Eqn. (4), and a local initial condition Eq. (6). However, constructing the computational model and solving it requires surmounting the following two major challenges:

1) Continuous deposition process: As the material is being added to the printed part, the computational domain continually increases at a rate contingent on the deposition speed, geometry, layer thickness, and deposition pattern.

*Time-dependent cooling surfaces*: The printing process causes a change in the bounding surfaces. In other words, the boundary conditions continually evolve depending on factors, such as deposition speed and part geometry. As the complexity of the part increases, tracking the elements related to the boundary surfaces becomes computationally burdensome.

The foregoing challenges imply that the time-varying computational domain and all the surfaces for initial and boundary conditions need to be determined *a priori* for a specific part.

## 3.2 Computational modeling of the heat transfer phenomena in the FFF process.

In this paper, the governing Eqn. (1) together with the boundary and initial conditions are solved using the Abaqus® commercial finite element method (FEM) software [37-40]. The part geometry is discretized using a custom-developed code. The deposition process is discretized in time as unit material depositions. The elements are numbered such that it is evocative of the deposition path encoded in the G-Code of the machine which informs the path taken by the extruder, and as a consequence, gradual activation of the local deposition is simplified.

The discrete deposition approach was implemented through activation of set of elements that constitute one deposition unit. As the deposition proceeds, new elements are activated in the computational mesh. The temperature of the activated nodes is initialized with the temperature matching the deposition temperature ( $T_d$ ). Further, the side and top surfaces of the deposited unit exposed to the environment are subjected to external convective and radiative heat transfer according to Eqn. (3). The location of the corresponding free surfaces is tracked in the user-defined Abaqus-specific subroutine called DFLUX. We note that even for a simple geometry and scan

pattern, tracking the free surface is fraught with complexity. For example, for a cuboid-shaped geometry, at any given time (t) the direction of the extruder is given by:

$$d = (-1)^{\left|\frac{t}{t_{road}}\right|} \tag{7}$$

where, d represents the direction of the print and  $t_{road}$  is the time required to deposit a single road  $(t_{road} = \frac{road \, length}{print \, speed \, (v)})$ . We use the direction d to first determine the position of the extruder during the deposition, next to guide the free surface tracking and finally to apply the boundary conditions. Formally, for the simple cuboid geometry of the part, the extruder position  $(x_e, y_e, z_e)$ , given in units of length (m), can be expressed as:

$$z_{e} = \left[ t/t_{layer} \right] \cdot h_{d}$$

$$x_{e} = \left[ \left( t - (H-1) \cdot t_{layer} \right) / t_{road} \right] \cdot w_{d}$$

$$y_{e} = \begin{cases} (t - \left[ t/t_{road} \right]) \cdot v_{d} & \forall d = 1 \\ B - (t - \left[ t/t_{road} \right]) \cdot v_{d} & \forall d = -1 \end{cases}$$
(8)

Once the position of the extruder is determined, the free surfaces and according boundary conditions can be applied for nodes with following coordinates (x, y, z):

$$x = 0 \text{ or } y = 0$$

$$x = L \text{ or } y = B$$

$$x < x_e \text{ and } z = z_e$$

$$d \cdot y < d \cdot y_e \text{ and } z = z_e \text{ and } x < x_e + l_d$$

$$(9)$$

where L is the length of the part for x direction and B is the breadth for y-direction as shown in Figure 3. The unit depositions are of size  $(l_d, b_d, h_d)$ , given in units of length (m). When a new set of elements is added to the mesh, the boundary conditions need to be updated accordingly. Specifically, for surfaces buried under just added set of elements the boundary conditions need to be removed, while for the free surfaces just exposed to the environment the boundary conditions must be added to the model.

### Please Enter Figure 3 Here.

The deposited roads have a cross-section of  $\approx 0.2 \text{ mm}^2$  that are discretized into four elements. With such fine discretization, the mesh for a print of a 25 cm<sup>3</sup> volume consists of approximately 1 million nodes. The mesh was generated to capture the thermal behavior without requiring considerably high computational effort, with size of element chosen through convergence analysis. The material properties are obtained from standard data sheets for ABS thermoplastic. The ambient temperature ( $T_{am}$ ) in Eqn. (3) is the environment temperature and is set to 303.15 K (30°C) during the printing process. All other material properties, process parameters, and simulation details are given in Table 1.

The computing time measured for our 10-layer simulation is approximately 21 hours on a 20 core CPU (Intel® Xeon® E5-2650 v3 @ 2.30GHz) with 62.5 GB RAM. Our scalability studies indicate that the computing time increases exponentially with the increase in the degrees of freedom of the system. The total number of degrees of freedom is proportional to the number of layers. Consequently, the computing time would exponentially increase with the number of layers. The computational tortuosity is the major impediment to the simulation of a large part with a high-fidelity model; we estimate that it will require approximately two weeks (on the same machine – 20 cores) to simulate a similar geometry with 100 layers.

## Please Enter Table 1 Here.

### 4 Experimental Validation

## 4.1 Sensing setup

In this work, we used a Hyrel Hydra FFF (by Hyrel3D) machine to print a sample part and acquire in-process data. We note the following characteristics intrinsic to the FFF process and machine used in this work, which imposes certain constraints on the thermal measurements that can be acquired. The first, and main, hurdle in sensing the surface temperature of a freshly deposited extrudate in FFF is the exceedingly small gap between table and tip of the nozzle, in this work the gap is 0.2 mm (standoff distance). The small gap between the build table and nozzle entails that bulky thermal imaging sensors, such as infrared cameras or pyrometers, commonly used in metal additive manufacturing processes, such as laser powder bed fusion and directed energy deposition will not be affective, as their field-of-view will be blocked by the nozzle. For instance, in laser powder bed fusion the entire bed is exposed to the laser, and in directed energy deposition, the standoff distance is typically 5 to 10 mm. Second, embedding thermocouples inside the build plate is not a viable strategy in FFF, in contrast to directed energy deposition, because the poor thermal conductivity of the polymer materials in FFF attenuate (weaken) the temperature signatures as successive layers are deposited, and the part grows in size.

Third, the build plate and nozzle move relative to each other at a high speed (typically 20 mm/s), which constrains the viability of using a static sensor as it becomes intractable to capture the surface temperature as soon the extrudate material is deposited. Taking the above constraints into account, the feasible solution is to use a sensing system that is non-contact, sufficiently compact to view the build plate, and is exceedingly light-weight so that the sensor can be mounted nearly-coaxial to the nozzle and can travel along with the nozzle as it translates back-and-forth without interfering the kinetics of the machine or imposing large inertial mass.

Accordingly, the Hyrel FFF machine used in this work is instrumented with three infrared K-type thermocouples sensors (Exergen-150046). Figure 4(a) and (b) show the schematic, and Figure 4(c) and (d) depict the actual sensing array implemented in this work. The infrared thermocouple sensors measure the absolute temperature and are calibrated for a linear response up to 200°C. The temperature measurements are acquired at a sampling rate of 10 Hz and conditioned through a National Instruments data acquisition (NI DAQ 9188) board. Thus, the data is time-stamped, and the data acquired is aligned to the position of the nozzle based on visual demarcation via continuous video feed acquired using an optical camera.

However, the tradeoff with using such as an infrared thermocouple sensor is that it has a fanbeam-type field-of-view. To explain further, the area over which the temperature is averaged increases as the distance of the active area of the sensor from the region of interest increases (i.e., the top of the extrudate), at the nearest possible distance the infrared thermocouple averages the temperature over a 24 mm² elliptical area. In an ideal scenario, the area measured would be a circular area having radius of one road width (~ 4 mm²). While the area measured in this work is an elliptical 24 mm² area, which is magnitude larger than that of an ideal measurement area, viz., the width of a road (~ 4 mm²), this constraint is inherent due to physical limitations of restricted space for location of sensors on the machine. To the best of our knowledge, this work is the first to use an in-situ measurement system capable of capturing the surface temperature of a freshly deposited extrudate, and which is mounted coaxial to the nozzle so that the measured temperature is within its immediately within its field-of-view.

### Please Enter Figure 4 Here.

Figure 5 shows the position of the middle infrared sensor, and the manner in which it records the temperature of an individual track of deposited material. As shown in Figure 5, the middle infrared sensor peers at the part at an angle, and hence, the area over which temperature is measured for a deposited track tends to be elliptical in shape. The measured area has the point of extrusion as the center and moves along with the extruder. Besides, the sensor also scans a portion of the extruder. To account for these eventualities, and reconcile the temperature data acquired by the sensors with the trends predicted by the thermal model, we further processed the sensor data to remove spurious effects.

### Please Enter Figure 5 Here.

To explain further, we averaged the temperature distribution predicted by the simulation over an elliptical area identical to the area scanned by the IR temperature sensor. This area (≈ 24 mm²) is estimated from a solid model reproduction of the experimental setup as shown in Figure 5, the middle IR sensor overlooks the print at an angle, which makes the area measured to be elliptical in shape. The area has the point of extrusion as the center and moves with the extruder. Besides, the sensor also scans a portion of the extruder and the base.

To account for the difference of temperature contingent on the scanned areas, we average the temperature distribution from the simulation follows:  $T = w_1 T_p + w_2 T_{ext}$ , where weights  $w_1 = 0.784$ , and  $w_2 = 0.216$  corresponds to: area fraction of the part and base, and area fraction blocked by the extruder, respectively. The area fraction corresponding to the field of view of the IR sensors blocked by the extruder is measured from the CAD model (Figure 5).

The CAD analysis shows 21.6% of the area measured by the IR sensor is covered by the extruder. We assume the extruder temperature  $(T_{ext})$  to be constant. The remaining area fraction

corresponds to the part and the base. The base temperature is assumed constant, while the part temperature  $T_p$  is predicted by the model. The area fraction covered by the part (and base) is time dependent and is linked to the movement of the extruder.

### 4.2 Test Geometry and Process Conditions Chosen for Experimental Validation

The test part shown in Figure 6 is used for empirical testing. It is essentially a two-tier stepped-pyramid type object. The test part has a total of 10 layers, each tier accounting for 5 layers; the layer height being 0.2 mm. We maintain all the processing parameters delineated in Table 2 constant. We note that the test part used embodies a change in the surface area with progressive deposition, which in turn has a consequential effect on the thermal history. In other words, instead of the same cyclical, repeating pattern in the temperature trends, the geometry shown in Figure 6 entails a time-varying part design-thermal pattern interaction.

## Please Enter Figure 6 Here.

#### Please Enter Table 2 Here.

The feed rate ( $\nu$ ) is varied at three levels of 20, 30 and 40 mm/s. The variation of the feed rate levels leads to change in the feed rate to flow rate ratio and is thus linked to the physical characteristics of the extrudate. A large feed rate to flow rate ratio results in so-called stringy deposition of the road. A stringly extrudate causes poor bonding between adjacent roads, and weakens the part. Whereas, a small feed rate to flow rate ratio causes inordinately thick roads to be deposited. If the height of the road exceeds the set layer thickness, the deposited material will make contact with the extruder leading to clogging of the extruder. The effect of feed rate to flow rate ratio thus has a discernible effect on the quality of the part. The effect of feed rate to flow rate ratio on the surface finish and nozzle clogging phenomena is discussed by Rao *et al.* [41]. Hence,

in this work the material flow rate is also adjusted so that the feed rate to flow rate ration is always unity (= 1).

Representative results from a process simulation depicting the progression of the temperature field as a function of the feed rate are shown in Figure 7. The figure shows the evolution of temperature field for three selected snapshots and three different feed rates. The left-most column of Figure 7 depicts the temperature distribution for the third layer of the first tier. The middle column of Figure 7 shows the temperature distribution for the first layer of the second tier. Finally, the right-most column of Figure 7 maps the temperature distribution of the second layer for the second tier.

## Please Enter Figure 7 Here.

It is observed from Figure 7 that the temperature distribution for the second layer is significantly different from the first tier. On average, the temperature rises by about 10° C. Specifically, for the second tier, the increased temperature zone is more widespread, which implies that the second tier of the part remains at a higher temperature for longer time. The high temperature may be advantageous as it will result in higher degree of bonding, as a polymer chain will have more time and energy to diffuse into adjacent roads and the preceding layer; inter-difussion is facilitated at highter temperature. For example, compare the columns for the time of 40 seconds for feed rate of 20 mm/s and 140 seconds for feed rate of 30 mm/s in Figure 7.

Next, the effect of feed rate on the thermal profile is further examined in Figure 8, which also comapres the measured surface temperature profiles with the model-derived predictions. The mean absolute percentage error (MAPE) and root mean squared error (RMSE) between the predicted temperature profile with FE-analysis and the measured temperature profile for the three feed rates studied are reported in Table 3.

#### Please Enter Table 3 Here.

### Please Enter Figure 8 Here.

The following inferences are drawn based on the temporal temperature trends reported in Figure 8.

- The surface temperature increases substantially for the second tier of the test artifact, compared to the first layer. This is because, given the smaller area of the second tier (15 mm × 15 mm), the extrudate has shorter time to cool between deposition of individual roads.
- The start of deposition in each layer corresponds to a periodic pattern, this periodic pattern occurs because the infrared thermocouple measures the average temperature over an area. As the layer cools, the average temperature over the rest of the area is lower than the currently deposited road.
- Within each layer a cyclical pattern is observed, this pattern corresponds to the deposition of an individual road within each layer. We note that material is deposited in one direction only, hence, after a hatch is deposited, the extruder returns to the starting position of the next hatch, without depositing material on the way back. As a consequence, the temperature drops on the return sojourn, as the material deposited is continually cooling.

From Figure 8 it is evident that the trends derived from the finite element (FE) model match the experimental data and location of the temperature spikes. The mean absolute percentage error (MAPE) is less than 6%, and root mean squred error (RMSE) is also within 6 °C. Pertinently, the close agreement in experimental and model-derived temperature profiles related to temporal location and trend in the signal is replicated across the different feed rates.

Moreover, the maximal root mean squared error of 10 °C occurs in the second tier, where the temperature is close to 150 °C, which is substantially above the glass transition temperature of the ABS material (approximately 110 °C). Hence, this temperature differential in the model and experiment is deemed inconsequential to govern the bonding behavior of adjacent tracks, called polymer reptation, which as explained in Section 3, governs the part strength.

More pertinent than the accuracy of predicting the absolute temperature is that the model correctly captures the thermal trends. This knowledge is the first step towards understanding the effect of part design and process parameters on the thermal history and through it the thermal-induced defects, such as distortion. For instance, using such a physical model is valuable for practitioners as they can anticipate *red flag* problems before the printing process is started, and use the knowledge to take remedial action, e.g., re-designing the part geometry or changing the process parameters, such as feed rate. Another outcome is this theoretical model is that serves as a baseline to monitor and establish feedback control of the process, as opposed to purely data-driven monitoring.

We posit that there are four main reasons for the discrepancy between the model and experimental data stemming from the small yet inherent stochasticity in the process.

- (1) The fan near the extruder switches on and off intermittently to protect the cartridge heater in the liquefier from overheating, this introduces a degree of forced convection and cooling of the surface.
- (2) The extruder is not always at a steady temperature; indeed, the temperature fluctuations can range as large as 5 °C in the setpoint before the controller activates to maintain the setpoint temperature. A similar control delay exists in the heater inside the bed.

- (3) The part tends to slightly warp upwards (U-shape), especially during the second tier, as a consequence of this distortion is that the standoff distance between the part and extruder will decrease during the process. As the standoff distance decreases, more heat is delivered to the part due to its closer proximity to the extruder mechanism.
- (4) Despite all precautions, the vibration intrinsic in the machine manifests in the fixture holding the infrared thermocouples, which in turn causes errors in the temperature measurement.

#### **5** Conclusions and Future Work

In this work we developed and applied a finite element-based transient model to explain the effect of the material feed rate on the instantaneous spatiotemporal distribution of temperature, called temperature history or thermal profile in parts made using the fused filament fabrication (FFF) additive manufacturing process. The thermal profiles predicted by the finite element model were experimentally validated on a Hyrel Hydra FFF machine integrated with multiple non-contact infrared thermocouple sensors. The main finding is that the temperature variations resulting from a change in the layer geometry of a test object, and due to the process condition (feed rate), were predicted using the FE model within 6% mean absolute percentage error, and 6 °C root mean squared error of experimental observations. This work, therefore, explains how and why the temperature profile in FFF is linked to the process parameters and part design. This knowledge is the foundational basis for determining the optimal part geometry and process conditions, as well as model-based closed-loop control of the FFF process [2].

Our future work in the area will endeavor to answer the following questions:

1. What is the effect of different materials, and more complex part geometries on the temperature profile?

- 2. What is the effect of the temperature profile on the bonding degree and functional properties of the part?
- 3. What should be the corrective action once a defect is detected, and how can such a corrective action be integrated with a theoretical model to realize feedforward process control?

### Acknowledgments

The authors thank the associate editor Dr. Kevin Chou and the three anonymous reviewers whose time, attention to detail, and helpful suggestions have doubtlessly improved the quality of this work. One of the authors (PKR) acknowledges the NSF for funding his research through the following grants CMMI-1719388, CMMI-1739696 and CMMI-1752069 (CAREER) at the University of Nebraska-Lincoln. Specifically, the concept of integrating in-process sensing, thermal modeling, and model-based defect detection and isolation was funded through CMMI-1752069 towards a *correct-as-you-build* smart additive manufacturing paradigm.

#### References

- [1] Bikas, H., Stavropoulos, P., and Chryssolouris, G., 2016, "Additive manufacturing methods and modelling approaches: a critical review," The International Journal of Advanced Manufacturing Technology, **83**(1-4), pp. 389-405.
- [2] Huang, Y., Leu, M. C., Mazumder, J., and Donmez, A., 2015, "Additive Manufacturing: Current State, Future Potential, Gaps and Needs, and Recommendations," Transactions of the ASME, Journal of Manufacturing Science and Engineering, 137(1), p. 014001.
- [3] Knapp, G. L., Mukherjee, T., Zuback, J. S., Wei, H. L., Palmer, T. A., De, A., and DebRoy, T., 2017, "Building blocks for a digital twin of additive manufacturing," Acta Materialia, **135**, pp. 390-399.
- [4] DebRoy, T., Zhang, W., Turner, J., and Babu, S. S., 2017, "Building digital twins of 3D printing machines," Scripta Materialia, 135, pp. 119-124.
- [5] Gibson, I., Rosen, D. W., and Stucker, B., 2010, Additive Manufacturing Technologies Rapid Prototyping to Direct Digital Manufacturing, Springer, Boston, MA
- [6] ASTM, 2012, "F42 Standard terminology for additive manufacturing technologies," ASTM International.
- [7] Bellehumeur, C., Li, L., Sun, Q., and Gu, P., 2004, "Modeling of bond formation between polymer filaments in the fused deposition modeling process," Journal of Manufacturing Processes, 6(2), pp. 170-178.

- [8] Duty, C. E., Kunc, V., Compton, B., Post, B., Erdman, D., Smith, R., Lind, R., Lloyd, P., and Love, L., 2017, "Structure and mechanical behavior of Big Area Additive Manufacturing (BAAM) materials," Rapid Prototyping Journal, 23(1), pp. 181-189.
- [9] Khoshnevis, B., 2004, "Automated construction by contour crafting—related robotics and information technologies," Automation in construction, **13**(1), pp. 5-19.
- [10] Talagani, M., DorMohammadi, S., Dutton, R., Godines, C., Baid, H., Abdi, F., Kunc, V., Compton, B., Simunovic, S., and Duty, C., 2015, "Numerical simulation of big area additive manufacturing (3D printing) of a full size car," SAMPE Journal, 51(4), pp. 27-36.
- [11] Turner, B., Strong, R., and Gold, S., 2014, "A review of melt extrusion additive manufacturing processes: I. Process design and modeling," Rapid Prototyping Journal, **20**(3), pp. 192-204.
- [12] Turner, B. N., and Gold, S. A., 2015, "A review of melt extrusion additive manufacturing processes: II. Materials, dimensional accuracy, and surface roughness," Rapid Prototyping Journal, 21(3), pp. 250-261.
- [13] Yardimci, M. A., Hattori, T., Guceri, S. I., and Danforth, S., 1997, "Thermal analysis of fused deposition," Proceedings of solid freeform fabrication conference, August, University of Texas, Texas, pp. 689-698.
- [14] Atif Yardimci, M., and Güçeri, S., 1996, "Conceptual framework for the thermal process modelling of fused deposition," Rapid Prototyping Journal, 2(2), pp. 26-31.
- [15] Rodríguez, J. F., Thomas, J. P., and Renaud, J. E., 2001, "Mechanical behavior of acrylonitrile butadiene styrene (ABS) fused deposition materials. Experimental investigation," Rapid Prototyping Journal, 7(3), pp. 148-158.
- [16] Zhang, Y., and Chou, Y., 2006, "Three-dimensional finite element analysis simulations of the fused deposition modelling process," Proceedings of the Institution of Mechanical Engineers, Part B: Journal of Engineering Manufacture, **220**(10), pp. 1663-1671.
- [17] Zhang, Y., and Chou, K., 2008, "A parametric study of part distortions in fused deposition modelling using three-dimensional finite element analysis," Proceedings of the Institution of Mechanical Engineers, Part B: Journal of Engineering Manufacture, 222(8), pp. 959-968.
- [18] Li, L., 2002, Analysis and fabrication of FDM prototypes with locally controlled properties, University of Calgary,
- [19] Rodriguez, M. J., 2000, "Modeling the mechanical behavior of fused deposition acrylonitrile-butadiene-styrene polymer components,"
- [20] Costa, S., Duarte, F., and Covas, J., 2015, "Thermal conditions affecting heat transfer in FDM/FFE: a contribution towards the numerical modelling of the process: This paper investigates convection, conduction and radiation phenomena in the filament deposition process," Virtual and Physical Prototyping, **10**(1), pp. 35-46.
- [21] Patil, N., Pal, D., Khalid Rafi, H., Zeng, K., Moreland, A., Hicks, A., Beeler, D., and Stucker, B., 2015, "A Generalized Feed Forward Dynamic Adaptive Mesh Refinement and Derefinement Finite Element Framework for Metal Laser Sintering—Part I: Formulation and Algorithm Development," Journal of Manufacturing Science and Engineering, 137(4), pp. 041001-041001-041015.
- [22] Pal, D., Patil, N., Kutty, K. H., Zeng, K., Moreland, A., Hicks, A., Beeler, D., and Stucker, B., 2016, "A Generalized Feed-Forward Dynamic Adaptive Mesh Refinement and Derefinement Finite-Element Framework for Metal Laser Sintering—Part II: Nonlinear

- Thermal Simulations and Validations2," Journal of Manufacturing Science and Engineering, **138**(6), pp. 061003-061003-061010.
- [23] Olleak, A., and Xi, Z., 2018, "Finite element modeling of the selective laser melting process for Ti-6Al-4V," Proceedings of the Solid Freeform Fabrication Symposium.
- [24] Zeng, K., Pal, D., Gong, H., Patil, N., and Stucker, B., 2015, "Comparison of 3DSIM thermal modelling of selective laser melting using new dynamic meshing method to ANSYS," Materials Science and Technology, **31**(8), pp. 945-956.
- [25] Gouge, M., Michaleris, P., Denlinger, E., and Irwin, J., 2018, "The Finite Element Method for the Thermo-Mechanical Modeling of Additive Manufacturing Processes," Thermo-Mechanical Modeling of Additive Manufacturing, Elsevier, pp. 19-38.
- [26] Yavari, M. R., Cole, K. D., and Rao, P., 2019, "Thermal Modeling in Metal Additive Manufacturing Using Graph Theory," Journal of Manufacturing Science and Engineering, 141(7), pp. 071007-071007-071020.
- [27] Yavari, M. R., Cole, K. D., and Rao, P. K., 2019, "Design Rules for Additive Manufacturing—Understanding the Fundamental Thermal Phenomena to Reduce Scrap," Procedia Manufacturing, **33**, pp. 375-382.
- [28] Bukkapatnam, S., and Clark, B., 2007, "Dynamic modeling and monitoring of contour crafting-: An extrusion-based layered manufacturing process," Transactions of the ASME, Journal of Manufacturing Science and Engineering, **129**(1), pp. 135-142.
- [29] Fang, T., Bakhadyrov, I., Jafari, M. A., and Alpan, G., 1998, "Online detection of defects in layered manufacturing," IEEE International Conference on Robotics and Automation, IEEE, pp. 254-259.
- [30] Cheng, Y., and Jafari, M. A., 2008, "Vision-based online process control in manufacturing applications," IEEE Transactions on Automation Science and Engineering, 5(1), pp. 140-153.
- [31] He, K., Wang, H., and Hu, H., 2018, "Approach to Online Defect Monitoring in Fused Deposition Modeling Based on the Variation of the Temperature Field," Complexity, **2018**
- [32] Wu, H., Yu, Z., and Wang, Y., 2017, "Real-time FDM machine condition monitoring and diagnosis based on acoustic emission and hidden semi-Markov model," The International Journal of Advanced Manufacturing Technology, **90**(5-8), pp. 2027-2036.
- [33] Seppala, J. E., and Migler, K. D., 2016, "Infrared thermography of welding zones produced by polymer extrusion additive manufacturing," Additive manufacturing, 12, pp. 71-76.
- [34] Dinwiddie, R. B., Love, L. J., and Rowe, J. C., 2013, "Real-time process monitoring and temperature mapping of a 3D polymer printing process," Thermosense: Thermal Infrared Applications XXXV, International Society for Optics and Photonics, p. 87050L.
- [35] Kousiatza, C., and Karalekas, D., 2016, "In-situ monitoring of strain and temperature distributions during fused deposition modeling process," Materials & Design, 97, pp. 400-406.
- [36] Bastien, L., and Gillespie Jr, J., 1991, "A non-isothermal healing model for strength and toughness of fusion bonded joints of amorphous thermoplastics," Polymer Engineering & Science, 31(24), pp. 1720-1730.
- [37] Bathe, K.-J., 2006, Finite element procedures, Klaus-Jurgen Bathe,
- [38] Hughes, T. J., 2012, The finite element method: linear static and dynamic finite element analysis, Courier Corporation,

- [39] Reddy, J. N., and Gartling, D. K., 2010, The finite element method in heat transfer and fluid dynamics, CRC press,
- [40] Strang, G., and Fix, G. J., 1973, An analysis of the finite element method, Prentice-hall Englewood Cliffs, NJ,
- [41] Rao, P. K., Liu, J., Roberson, D., Kong, Z., and Williams, C., 2015, "Online Real-Time Quality Monitoring in Additive Manufacturing Processes Using Heterogeneous Sensors," Journal of Manufacturing Science and Engineering, 137(6), pp. 061007-061007-061012.

### **List of Figures and Figure Captions**

- Figure 1. A schematic of the fused filament fabrication (FFF) AM process.
- Figure 2: The salient heat transfer phenomena in FFF process stratified per the five interaction zones.
- Figure 3: Discretized deposition pattern implemented in this work. Two deposition directions are considered (left panel: positive direction, right panel: negative direction). The figure depicts the auxiliary quantities used to determine the local position of the extruder and the coordinates required to update boundary conditions and initiate the temperature of just added or activated elements.
- Figure 4. (a) and (b) schematic diagram of the setup, (c) and (d) photograph of the actual implementation.
- Figure 5. (a) Position of the middle infrared sensor to the extruder, (b) the covered area of the extruded material and hot extruder by the middle infrared sensor.
- Figure 6. Geometry of the stepped pyramid-shaped test artifact studied in this work. This particular part geometry has two tiers, the second of which has a smaller surface area than the first. As a result, the thermal patterns will vary as the part is being deposited.
- Figure 7: Temperature distribution snapshots captured during the FE-simulation of the deposition process for different feed rates. The left-most column shows the approximate middle of the third of five layers of the first tier of the test artifact. The middle column captures the first layer of the second tier (sixth layer overall), and the right-most column depicts the second layer of the second tier (seventh layer overall). These snapshots reveal the intertwined nature of the feed rate and thermal history.
- Figure 8. The experimental data (thick lines) are compared with the FE-model derived predictions (dotted line) for different feed rates (f<sub>r</sub>). The top row (a1) through (c1) shows the overall trends; the bottom row (a2) through (c2) shows a zoomed in portion highlighted in the top row.

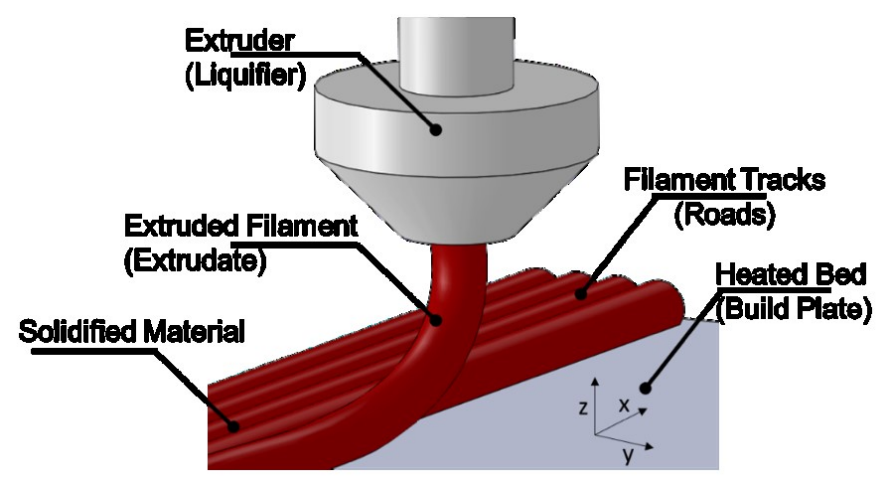


Figure 1. A schematic of the fused filament fabrication (FFF) AM process.

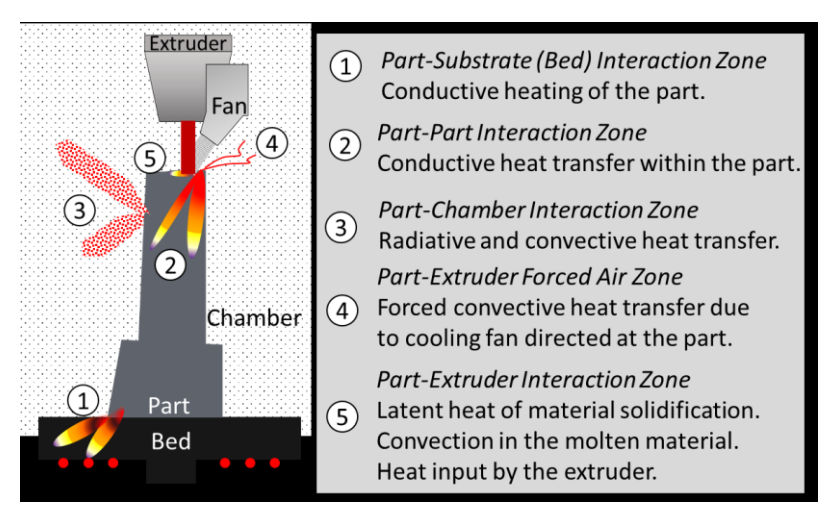


Figure 2: The salient heat transfer phenomena in FFF process stratified per the five interaction zones.

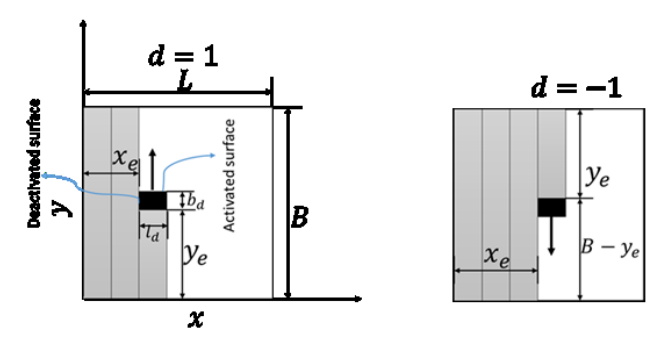


Figure 3: Discretized deposition pattern implemented in this work. Two deposition directions are considered (left panel: positive direction, right panel: negative direction). The figure depicts the auxiliary quantities used to determine the local position of the extruder and the coordinates required to update boundary conditions and initiate the temperature of just added or activated elements.

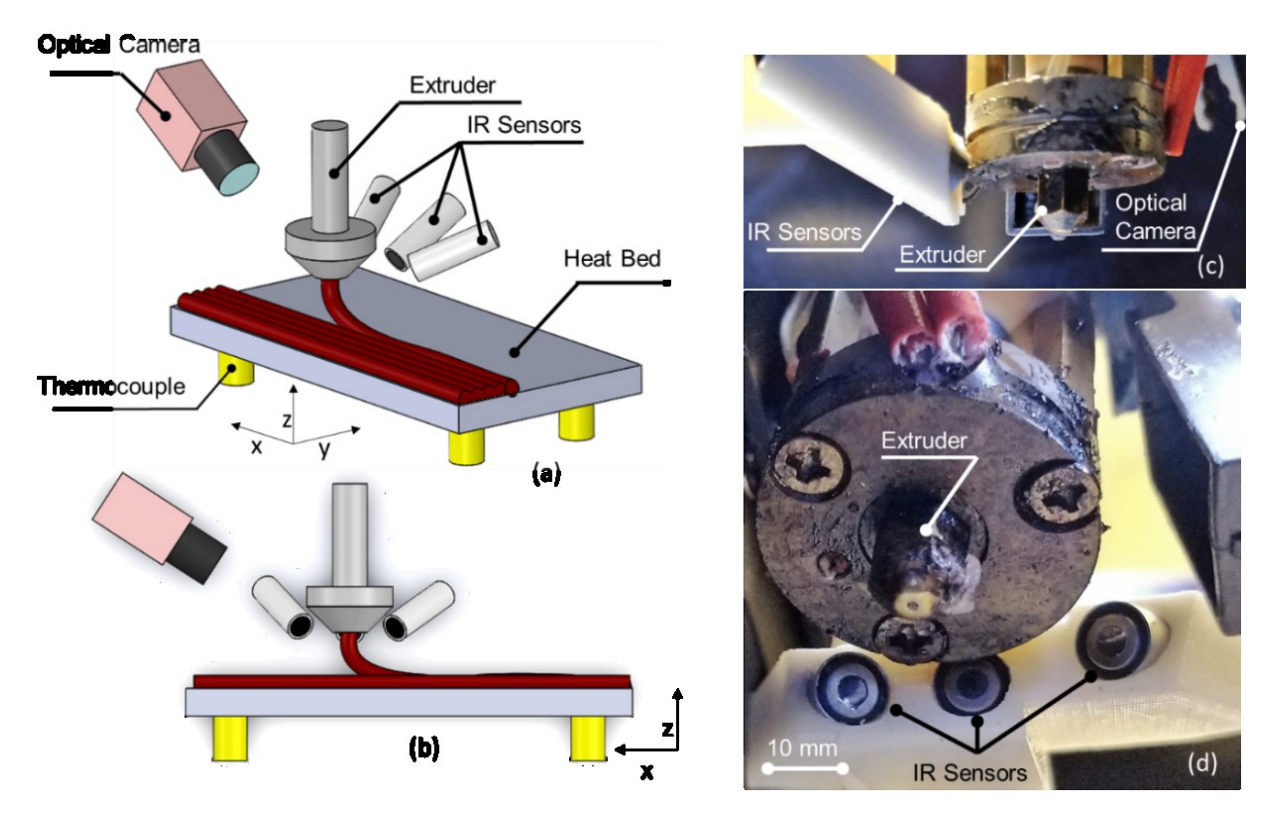


Figure 4. (a) and (b) schematic diagram of the setup, (c) and (d) photograph of the actual implementation.

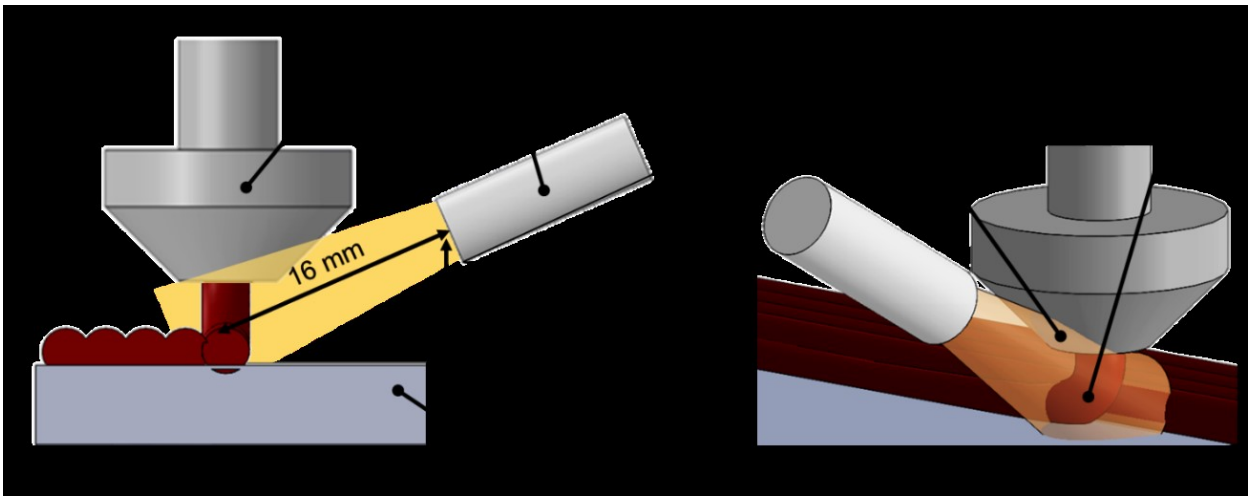


Figure 5. (a) Position of the middle infrared sensor to the extruder, (b) the covered area of the extruded material and hot extruder by the middle infrared sensor.

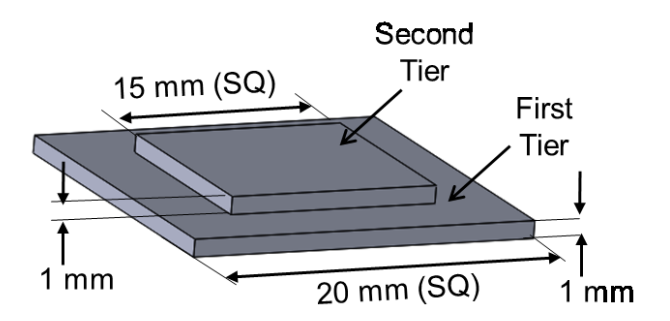


Figure 6. Geometry of the stepped pyramid-shaped test artifact studied in this work. This particular part geometry has two tiers, the second of which has a smaller surface area than the first. As a result, the thermal patterns will vary as the part is being deposited.

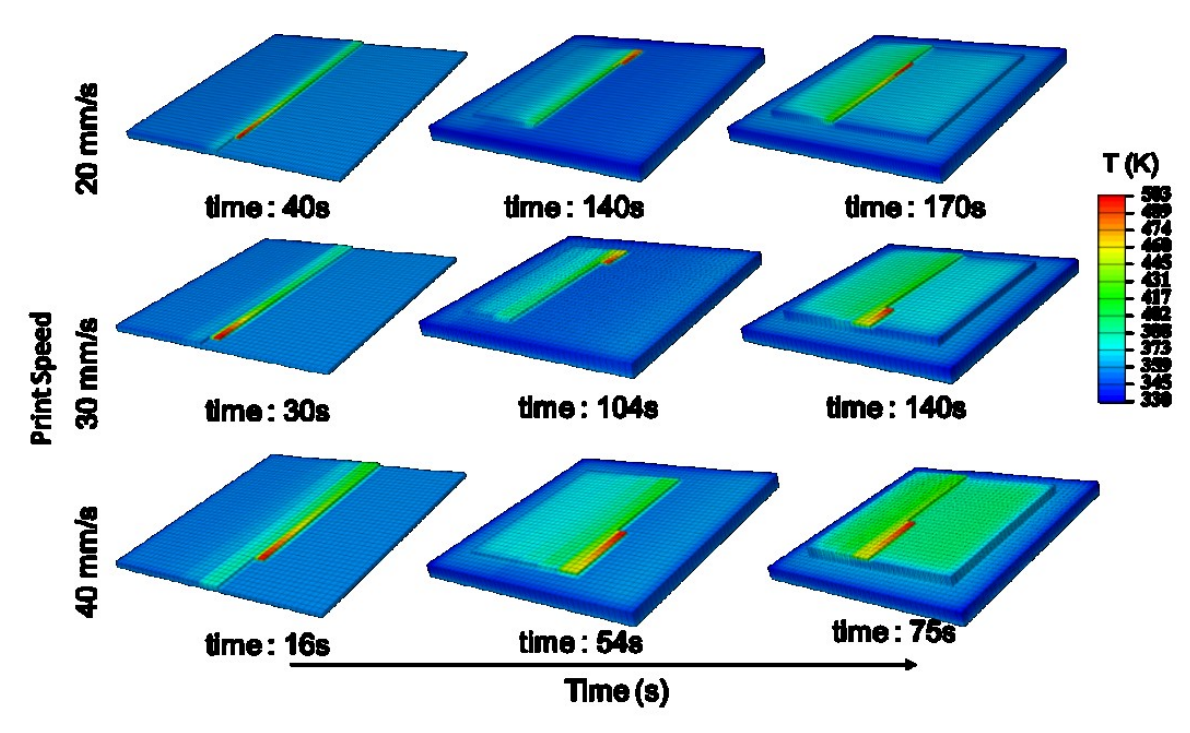


Figure 7: Temperature distribution snapshots captured during the FE-simulation of the deposition process for different feed rates. The left-most column shows the approximate middle of the third of five layers of the first tier of the test artifact. The middle column captures the first layer of the second tier (sixth layer overall), and the right-most column depicts the second layer of the second tier (seventh layer overall). These snapshots reveal the intertwined nature of the feed rate and thermal history.

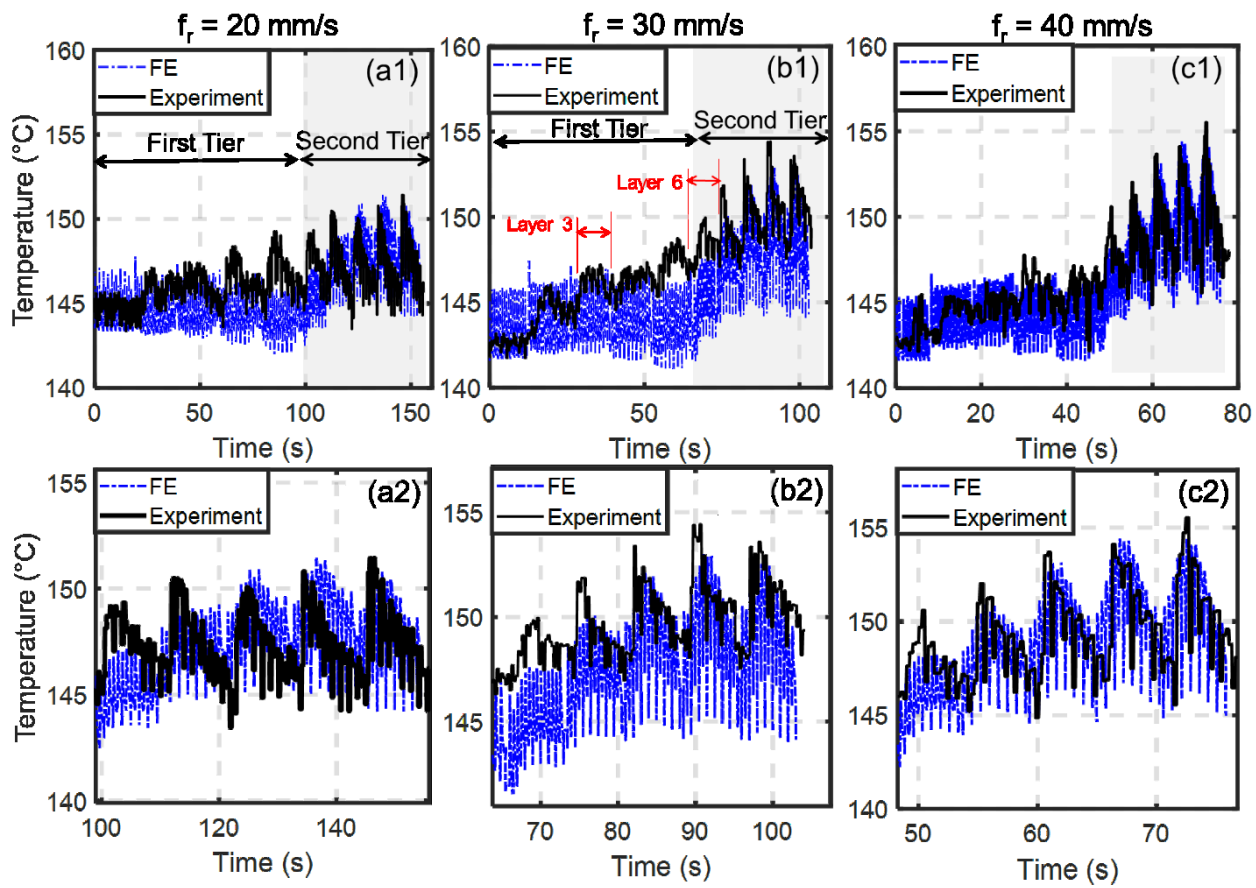


Figure 8. The experimental data (thick lines) are compared with the FE-model derived predictions (dotted line) for different feed rates  $(f_r)$ . The top row (al) through (cl) shows the overall trends; the bottom row (al) through (cl) shows a zoomed in portion highlighted in the top row.

# **List of Tables and Table Captions**

- Table 1: ABS material specific parameters, and simulation hyper parameters used in this work.
- Table 2. Printing Parameters that are maintained constant during experimentation.
- Table 3. Comparison of predicted temperature with FE and measured temperature from experiments in different feed rate conditions.

Table 1: ABS material specific parameters, and simulation hyper parameters used in this work.				
Material Properties	Conduction coefficient $(\lambda)$	0.17 W/m/K		
	Density $(\rho)$	$1050 \text{ kg/m}^3$		
	Specific heat $(c_p)$	2020 J/kg/K		
	Emissivity for air $(\kappa)$	0.90		
	Convection coefficient (h)	$21 \text{ W/m}^2/\text{K}$		
Process	Ambient temperature $(T_{am})$	303.15 K		
	Base temperature $(T_b)$	358.15 K		
	Print speed $(v)$	0.02, 0.03, 0.04  m/s		
	Layer Thickness	0.0002 m		
	Road Width	0.001 m		
Simulation Details	Element size	$0.0001 \times 0.0001 \times 0.0001 \text{ m}^3$		
	Element type	8 node linear thermal brick		
	Element type	element (DC3D8)		
	Integration	Full integration		
	Initial Condition	503.15 K		
	Activation set size	$0.0004 \times 0.0001 \times 0.0002 \text{ m}^3$		

Table 2. Printing Parameters that are maintained constant during experimentation.

Parameter	Value	Parameter	Value
Deposition width	1 mm	Layer thickness	0.2 mm
Scanning speed (feed rate, $(v)$ )	20, 30, 40 mm/s	Nozzle temperature	503.15 K
Hatch pattern	Linear	Ambient temperature $(T_{am})$	303.15 K
Bed temperature $(T_b)$	358.15 K	Material flow rate	20, 30, 40 mm/s
Total number of layers	10	Infill	100%

Table 3. Comparison of predicted temperature with FE and measured temperature from experiments in different feed rate conditions

Feed rate	20 mm/s	30 mm/s	40 mm/s
Mean Absolute Percentage Error (MAPE)	5.4%	5.8%	4.7%
Root Mean Square Error (RMSE, °C)	3.6	5.5	3.1